New Features In LS-DYNA

Editor: Yanhua Zhao yanhua@feainformation.com

SEPTEMBER FEATURED

Improvement of Mesh Fusion in LS-DYNA -
H.Fan, X. Zhu, L. Zhang and Y. Xiao
A 3D bond-based peridynamics model for dynamic brittle failure analysis in LS-DYNA®
B. Ren, C.T Wu

August

Conversion between FLD and Stress Triaxial Limit Curve
X. Zhu, L. Zhang, Y. Xiao
A non-orthogonal material model of woven composites in the preforming process -
W. Zhang, H. Ren, B. Liang, D. Zeng, X.Su, J. Dahl, M. Mirdamadi, Q. Zhao, J. Cao

July

Best Fit GUI for Metal Forming in LS-PrePost® 4.5
Q. Yan, X. Zhu, P. Ho, L. Zhang, Y. Xiao - LSTC
Modeling and Numerical Simulation of Afterburning of Thermobaric Explosives In a Closed Chamber
KS Im, G. Cook, Jr., and ZC Zhang - LSTC

June

Improvement of Sandwich Structure Part Adaptivity in LS-DYNA
Xinhai Zhu, Houfu Fan, Li Zhang and Yuzhong Xiao - LSTC
New Inflator Models in LS-DYNA®
Kyoung-Su Im, Zeng-Chan Zhang, and Grant O. Cook, Jr. - LSTC

May

Improvement of Mesh Fusion in LS-DYNA
Houfu Fan, Xinhai Zhu, Li Zhang and Yuzhong Xiao - LSTC
Representative Volume Element (RVE) analysis using LS-DYNA
C.T. Wu, W. Hu LSTC

April

New features of 3D adaptivity in LS-DYNA -
W. Hu LSTC
New Feature: Defining Hardening Curve in LS-DYNA® -
X. Zhu, L. Zhang, Y. Xiao

March

Improvements toOne-Step Simulation in LS-DYNA
Xinhai Zhu, Houfu Fan, Li Zhang,

February

LS-DYNA Smooth Particle Galerkin (SPG) Method
C.T. Wu, Y. Guo, W. Hu - LSTC

January

Lancing features in LS-DYNA
Quanqing Yan, Li Zhang, Yuzhong Xiao, Xinhai Zhu, Philip Ho - LSTC

LSTC Recent Developments, Features, Updates, News, Presentations

2016

December

Thermal Coupling Method Between SPH Particles and Solid Elements in LS-DYNA
Jingxiao Xu, Jason Wang, LSTC

November

Introduction to second order Lagrangian elements in LS-DYNA
Hailong Teng - Livermore Software Technology Corp.

October

*An Introduction to *CONSTRAINED_BEAM_IN_SOLID*
Hao Chen - Livermore Software Technology Corp

September:

Introduction to the new framework for User Subroutine Development of LS-DYNA
Zhidong Han and Brian Wainscott
*New Features in *ELEMENT_LANCING*
Xinhai Zhu, Li Zhang, Yuzhong Xiao

August :

Equivalent Radiated Power calculation with LS-DYNA
Yun Huang, Zhe Cui - Livermore Software Technology Corporation

July:

Recent Developments for Laminates and TSHELL Forming
Xinhai Zhu, Li Zhang, Yuzhong Xiao - LSTC

Improvement of Mesh Fusion in LS-DYNA

Houfu Fan, Xinhai Zhu, Li Zhang and Yuzhong Xiao
LSTC

ABSTRACT

In this work, mesh fusion in MPP is successfully implemented in LSDYNA®. It has been demonstrated through benchmark examples that MPP mesh fusion can reduce the simulation time (25%) and make sure the accuracy (error within 2%) of the forming process. The result for the corresponding spingback analysis is slightly large (error within 10%) and can serve as a rough and quick estimation.

INTRODUCTION

To improve simulation efficiency, mesh fusion has been implemented in LSDYNA® for a while. However, the implementation was only available in SMP, and its usage was very limited. Recently, mesh fusion has been successfully extended to MPP, and it can be activated with the existing keyword *CONTROL_ADAPTIVE through appropriate parameters NCFREQ, ADPCTL, CBIRTH and CDEATH.

The paper is organized as follows. The keyword to activate the MPP Fusion feature is first introduced. Numerical investigation with the NUMISHEET' 93 Benchmark is then conducted. Conclusion is drawn in the very end.

The Keyword *CONTROL_ADAPTIVE

Originally, adaptive fusion was implemented in SMP version. The MPP fusion feature was turned off with a warning message displayed at the beginning of any simulations that require fusion in MPP. As of Revision 113867, the MPP fusion is fully incorporated into the system.

The following keyword is the input to use the fusion feature.

```
*CONTROL_ADAPTIVE
$  ADPFREQ    ADPTOL    ADPOPT    MAXLVL    TBIRTH    TDEATH     LCADP    IOFLAG
    2.00      4.0         2         3         0.0       70.0       0         1
$  ADPSIZE    ADPASS    IREFLG    ADPENE    ADPTH     MEMORY     ORIENT   MAXEL
 0.0000000         1         0    5.000     0.0
$  IADPN90    IADPGH    NCFREQ    IADPCL    ADPCTL    CBIRTH     CDEATH   LCLVL
      -1         0         2         0        8.0      0.00       70.0
```

In the keyword, NCFREQ defines the fusion frequency, ADPCTL defines the fusion criterion, CBIRTH and CDEATH defines when the fusion starts and ends.

Numerical Investigation

To test the performance of the new feature, a number of simulations were carried out using the NUMISHEET'93 Benchmark, as shown in Figure 1. For each case, a forming process is first conducted, followed by the corresponding springback analysis. The simulations are first carried out in MPP with number of CPUs being 10. The performance comparison of the code with and without fusion is conducted. Specifically, we would like to check the differences in the simulation CPU time in the forming process, results in final springback angle, maximum effective plastic strain and minimum shell thickness in the workpiece with different number of CPUs running in MPP for cases with and without mesh fusion. As an illustration, the final mesh sizes and shapes of the springback angles running with 10 CPUs in MPP with and without mesh fusion are given in Figure 2. The differences of the two final springback angles are calculated to be 8.1%. In addition, the contours of the final shell thickness and effective plastic strains are provided in Figures 3 and 4, respectively. The difference in the minimum shell thickness is 1.4% and in the maximum effective plastic strain is 1.7%. The simulation time reduction is around 25% (not shown in the Figure).

To have a better view on the performances of the feature over different number of CPUs running in MPP, the forming process and springback analysis were carried out with the number of CPUs ranging from 1 to 35. Time costs of the cases with and without mesh fusion are shown in Figure 5(a), and the corresponding springback angles are given in Figure 5(b). Time reduction, differences in springback angle, minimum shell thickness and maximum effective plastic strain are shown in Figures 6(a), 6(b), 7(a) and 7(b), respectively. One can see that the overall time reductions in the forming processes are in general greater than or equal to 25%. The differences in springback angles are kept within 10%; the differences in the minimum shell thicknesses and maximum effective plastic strains are always kept within 2%, which means they are not affected significantly by the mesh fusion.

CONCLUSION:

The mesh fusion feature is successfully implemented in MPP and available for use. The fusion feature reduces the computation time notably (around 25%) and has little effects on formability analysis, such as thinning and effective strain predictions. The difference in the corresponding springback results is also found to be smaller than10%. The performance and accuracy studies can guide users in applying this new technology in a production simulation environment. Generally speaking, we should feel comfortable to use the fusion feature extensively in all formability related simulation since the leading indicators (shell thickness and effective plastic strain) affecting formability is little affected but one can achieve a speed-up factor of 25% in simulation turnaround. In springback simulation, however, one should approach it with caution. One can apply the feature if the springback results are to be used for a quick and rough estimation. However, if the results are to be used for compensating dies and in deciding how much tools are going to be re-machined, then its application may not be appropriate. The factor that people have higher expectation for springback simulation accuracy, now in the sub-millimeter when compared with physical scanned panel, should be taken into consideration when applying the feature in different scenarios.

In addition, the CPU time reduction can be affected by different model size.

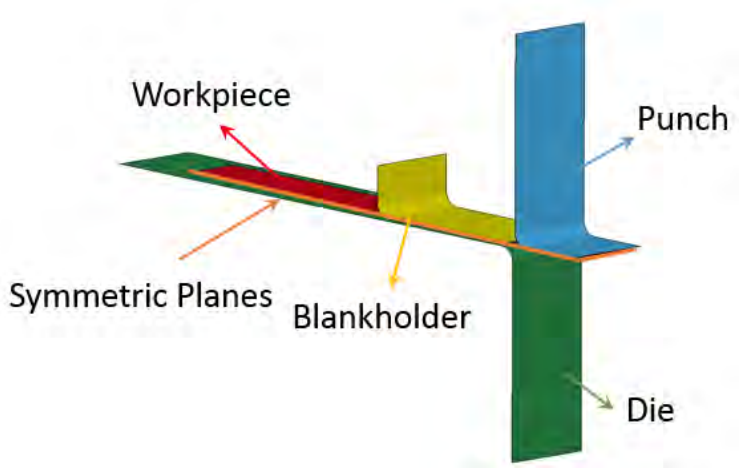

Figure 1. NUMISHEET'93 Benchmark: The punch, die and blankholder are rigid; the workpiece is discretized into shell elements. A forming process is conducted, followed by a springback analysis.

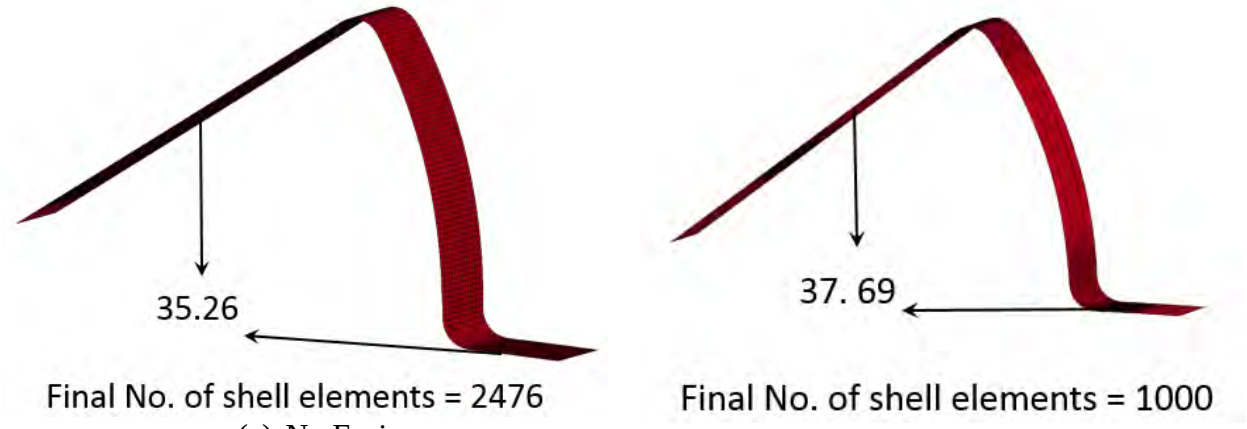

(a) No Fusion (b) With Fusion

Figure 2. The final number of elements and springback angles of the workpiece running with 10 CPUs in MPP.

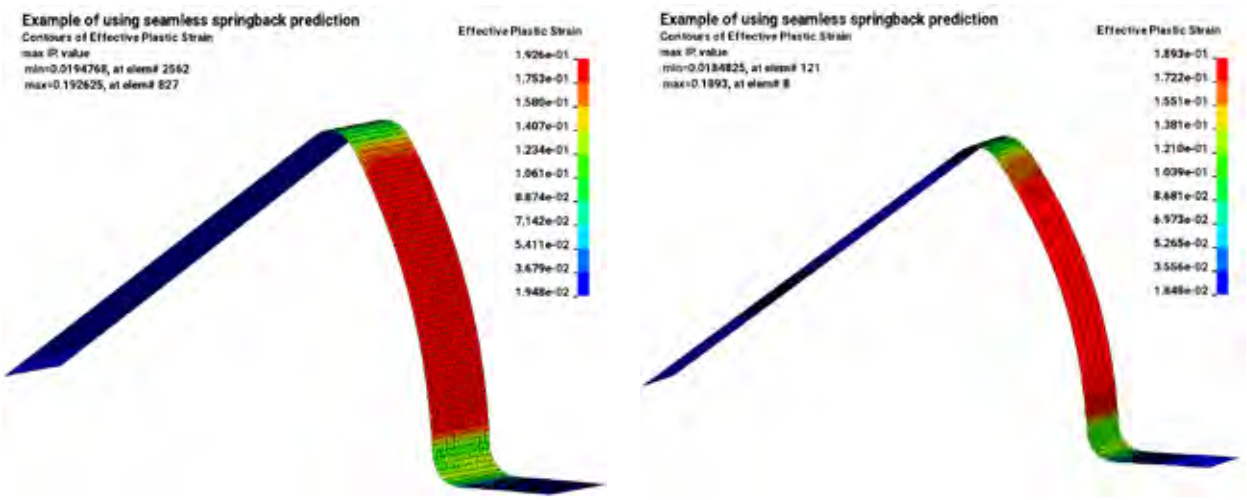

(a) No Fusion (b) With Fusion

Figure 3. The final effective plastic strain contours of the workpiece running with 10 CPUs in MPP.

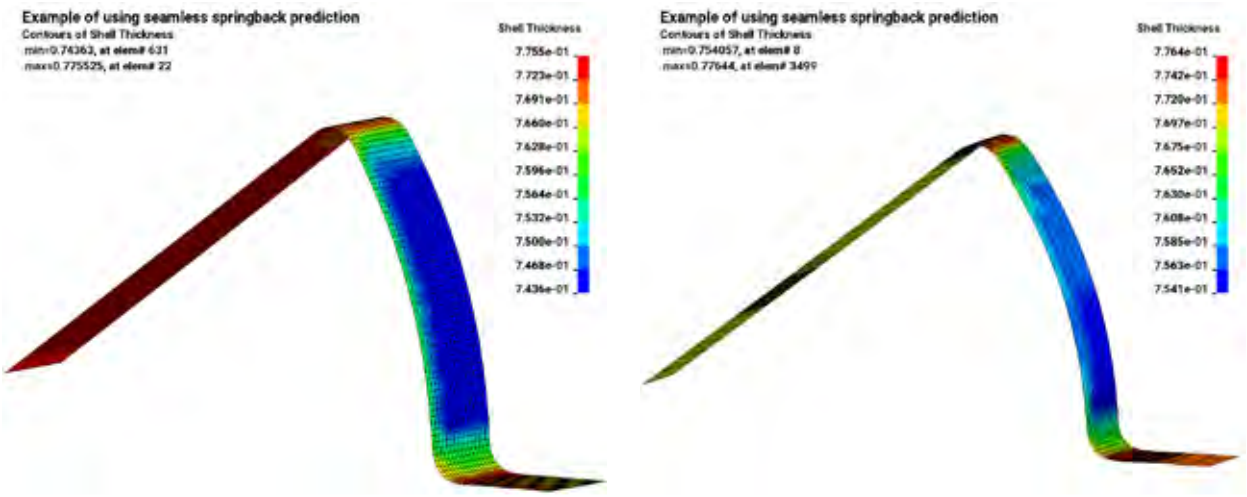

(a) No Fusion (b) With Fusion

Figure 4. The final shell thickness contours of the workpiece running with 10 CPUs in MPP.

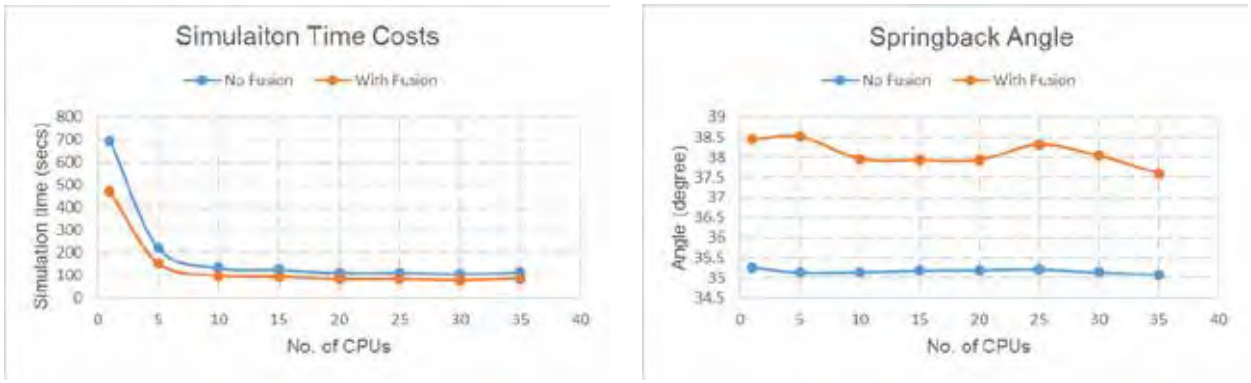

(a) Simulation time (b) Springback angle

Figure 5. Comparisons of the simulation CPU time and springback angles in MPP with different number of CPUs, with and without mesh fusion.

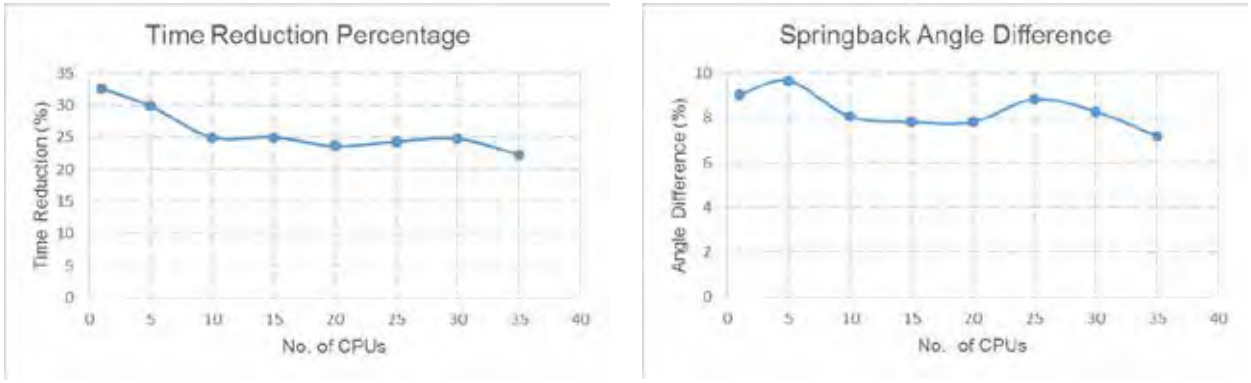

(a) Time Reduction (b) Springback Angle Difference

Figure 6. Time reduction and springback angle differences in MPP with different number of CPUs, with and without mesh fusion.

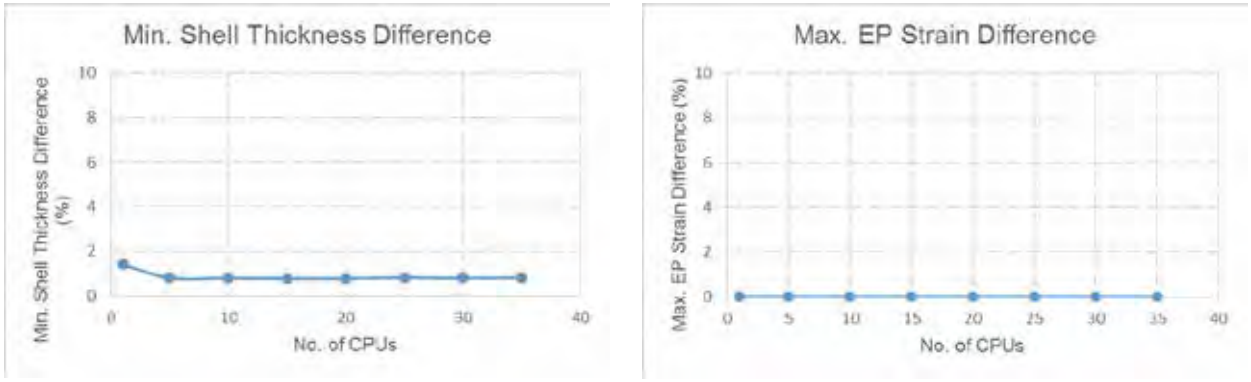

(a) Min. Shell Thickness Difference (b) Max. EP Strain Difference

Figure 7. Min. shell thickness and max. effective plastic strain differences in MPP with different number of CPUs, with and without mesh fusion.

ACKNOWLEDGEMENT:

The feature in this article was requested by BMW. Their valuable feedback during the development is highly appreciated.

REVISION INFORMATION:

MPP fusion feature is available starting in Revision 113867.

A 3D bond-based peridynamics model for dynamic brittle failure analysis in LS-DYNA®

Bo Ren, C. T Wu

Livermore Software Technology Corporation, 7374 Las Positas Road, Livermore, CA 94551

1. Introduction

The motivation of the peridynamics theory is the prediction of material damage in a 3D solid. Thus the peridynamics computational space is firstly partitioned by a set of material particles. Subsequently, the nonlocal integral term of peridynamics theory is implemented by the nodal integral approach [1]. An alternative way to perform the spatial integration and avoid those numerical defects in peridynamics models is constructing an approximation field of the kinematic quantity by finite element (FE) shape function [2, 3]. The FEM peridynamics approach inherits the advantages of FEM method such as the straightforward boundary condition enforcement and the robustness in non-uniform discretization. To represent the strong discontinuities in FEM peridynamics, the continuous approximation field is replaced by a piecewise continuous field which results in a discontinuous Galerkin formula for peridynamics [3].

This paper presents the explicit dynamics bond-based peridynamics formulas using the FEM discontinuous Galerkin theory. This paper is organized as follows. In section 2, the keywords for LS-DYNA® peridynacmis model are presented. Section 3 presents several benchmark problems. Final remarks are given in Section 4.

2. Keywords for the bond-based peridynamics model in LS-DYNA®

The bond-based peridynamics model in LS-DYNA® is implemented in FEM framework with discontinuous Galerkin theory. It is a new element formulation, therefore, a keywords is need to define the peridynamic section:

- *SECTION_SOLID_PERI (Available in R10., MPP, SMP)

This keyword has two parameter cards:

Card 1

Variable	SECID	ELFORM
Type	I	I
Default		

SECID: The section ID

ELFORM: Element formulation. Equals 48. Peridynamic section supports TET, PENT, HEX solid elements. Comparing with the regular FEM mesh, peridynamic computational mesh uses discontinuous mesh, i.e., each element has its own node index, the adjacent elements don't share nodes as Fig. 1. This discontinuous mesh can be built from a regular FEM mesh by detach nodes in LS-PrePost®

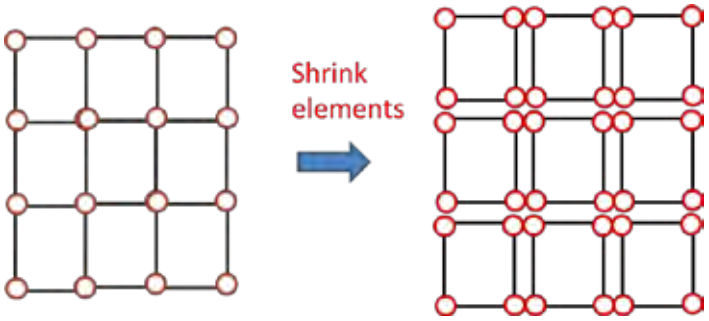

Fig. 1 Discontinous mesh for peridynamic model

Card 2

Variable	DR	PTYPE
Type	F	I
Default	1.01	1

DR: normalized horizon size, 1.0 is recommended

PTYPE EQ.1: bond based formulation

DR is the user defined reference support size which is normalized with the maximum element diagonal length. For those extreme irregular mesh, LSDYNA will adjust DR automatically to make sure the neighbor number of a point is $10 \leq n_g \leq 136$.

– *MAT_ELASTIC_PERI (available in R10.0, MPP, SMP)

This keyword defines a elastic material for peridynamic section, which is the only material model available for peridynamic section, and has one parameter card:

Card 1

Variable	MID	RO	E	G_T	G_S
Type	I	I	F	F	F
Default				1.0E20	$1.0e20$

RO: material density

E: Young's modulus

G_T: fracture energy release rate

G_s: fracture energy release rate for compression

Where G_T is the energy release rate G for the material (glass, cement, hard plastic etc.) in the material hand book. G_s is a numeric failure criteria for the compression dominated problems and G_s=2.0*G_T for those cases. For other problems, just leave blank.

3. Numerical examples

3.1 Mixed mode fracture in the three point bending problems

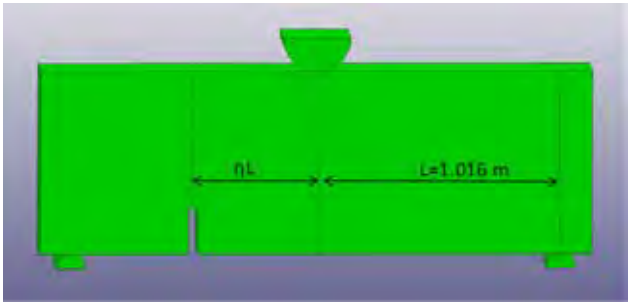

Fig. 2. The configuration of three point bending test

In this simulation, the three point bending tests of a pre-notched concrete beam are carried out. The configuration of the specimen and the position of notch are shown in Fig. 10 as the experimental set up [4]. The dimension of the specimen is $228.6mm \times 76.2mm \times 25.4mm$ supported by two fixed cylinders (radio: 6mm). The specimen is impacted by a cylinder projector with initial velocity: $0.05m/s$. According to the different position of notches (height:19.05mm), there are 3 cases of simulation are carried out which represent the mode-I fracture ($\eta = 0$ in Fig. 2) and the mixed mode fractures ($\eta = 0.5\ and\ \eta = 0.7$) respectively. The material properties of concrete are: $E = 29Gpa, \rho = 2400kg/m^3$ and Fracture energy release rate: $G = 31.1\,J/m^2$. The two support cylinders and the impactor are consider are considered as the rigid bodies. The specimen is partitioned by 27800 elements in each case. With different notch positions, the experimental tests show the tilted cracks with different angles, as Fig. 3. The case with $\eta = 0$ shows vertical crack and the cases ($\eta = 0.5\ and\ \eta = 0.7$) have the tilted crack path with angle: ($\theta = 22^0\ and\ \theta = 30^0$) respectively. The numerical simulations of these cases are plotted in Fig. 4 which illustrate a similar crack pattern with the angle 0^0 for $\eta = 0$; 21^0 for $\eta = 0.5$ and 29^0 for $\eta = 0.7$. This validation shows that the present method captures the fracture pattern well for the mode I and mixed modes.

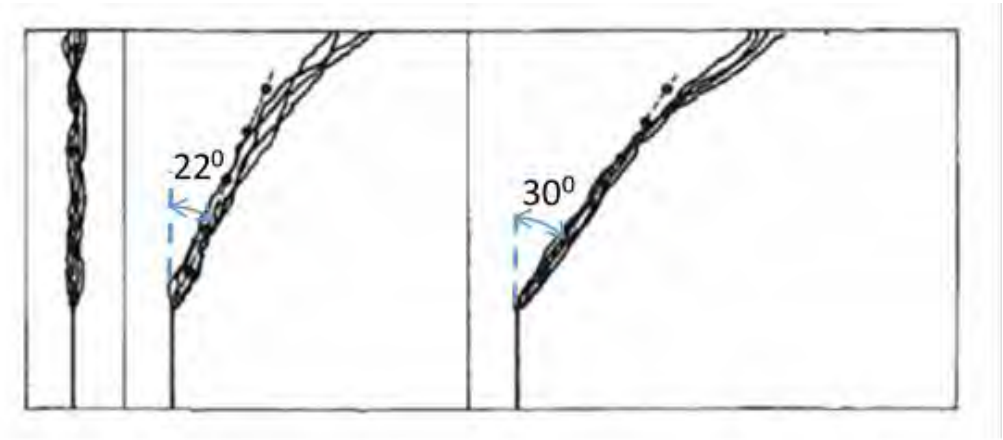

Fig. 2. Experimental crack paths under impaction [28]

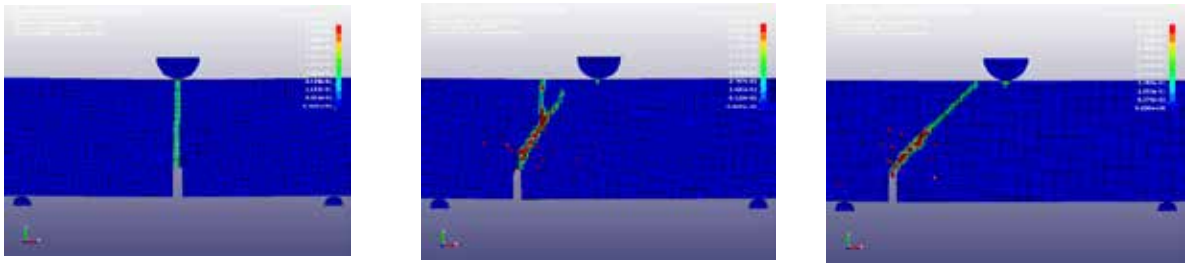

(a) $\eta = 0$ (b) $\eta = 0.5$ (c) $\eta = 0.7$

Fig. 3. The numerical predicted crack paths

3.2 Impact damage on the glass-polycarbonate-glass structure

One of the major applications of the bond-based peridynamics is the damage prediction of windshield in the crashworthiness simulation. The automobile windshield is made of a three-layer structure (glass-polycarbonate (pc)-glass) as shown in Fig. 4. The glass is soda-lime glass with material properties given by: $\rho = 2.44E3\ kg/m^3,\ E = 72Gpa,\ G = 8.0\ J/m^2$ [5]. The projectile is treated as a rigid body with material constants given by $\rho = 3.73E3\frac{kg}{m^3}$, $E = 210Gpa,\ \upsilon = 0.3$. This density leads to a total mass of $0.692\ g$ for projector. The projector is placed nearby the middle of the top surface with the initial velocity: $V_z = -31.0m/s$. Because no damage is observed in the PC layer from experiments [5], the PC layer is considered a simple elastic material with $\varrho = 1.2E3\ kg/m^3, E = 2.0Gpa,\ \upsilon = 0.25$.The glass-PC-glass specimen is discretized by 100,000 elements for glasses, 2500 elements for PC layer and the projector is simulated by one layer of brick elements at surface with 1014 elements shown in Fig. 4.

The damage patterns of the specimen are shown in Fig 5. Most damage patterns observed in the experiment are reproduced in this numerical simulation: the ripple cracks in the ellipses, the splitting cracks in the circles, through-thickness tilted cracks in the diamonds and boundary cracks in triangles. On the top surface of the glass, the main failure pattern consists of diagonal cracks and circle cracks nearby the impact zone. At the bottom surface, there is a main damage circle zone and the diagonal cracks extend from this zone as shown Figs. 6 (a) and (b). This damage pattern is well recognized in the failure analysis of windshield applications.

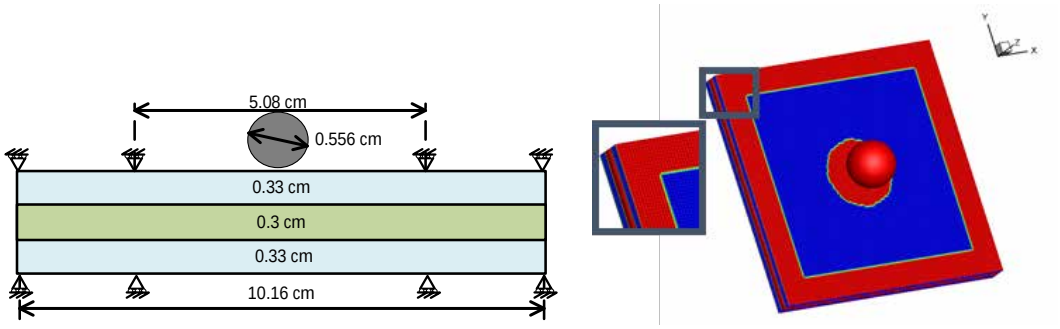

Fig. 4. The glass-PC-glass structure and computational model

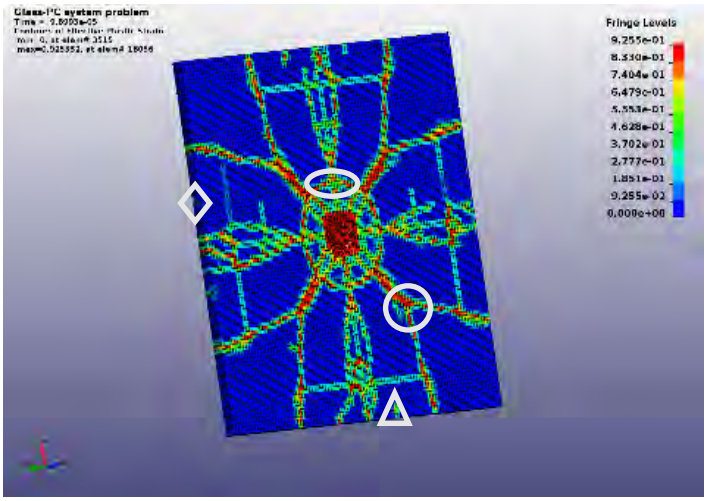

Fig. 5. Damage pattern in the glass

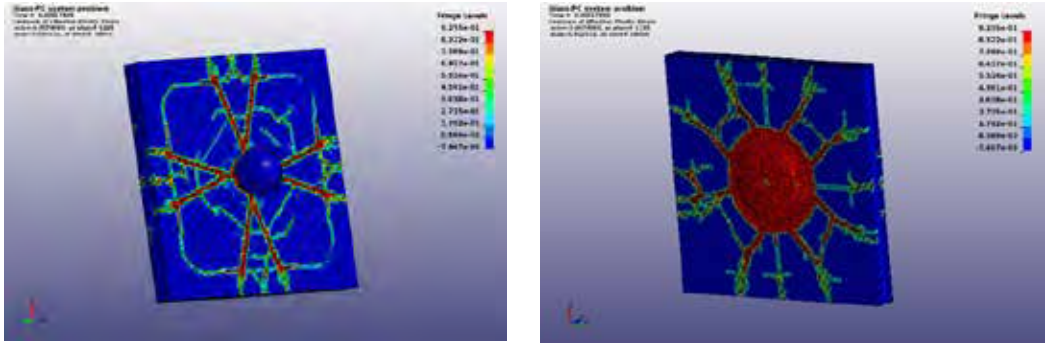

(a) (b)

Fig. 6. The damage status by impaction, (a) the top surface; (b) the bottom surface

4. Conclusion

This paper presents the usage of the 3D peridynamic model in LS-DYNA®. The numerical results suggest that this method can capture the dynamic response of elastic solid by the classic FEM method before damage occurs. The method can also predict the 3D dynamic process of mixed modes fracture, multi-cracks fracture and fragmentation effectively and accurately during the damage process.

References

[1] Silling SA, Askari E. A meshfree method based on the peridynamic model of solid mechanics. Computers and Structures 2005:83:1526–1535.

[2] Macek RW, Silling SA. Peridynamics via finite element analysis. Finite Elements in Analysis and Design 2007:43:1169-1178.

[3] Chen X, Gunzburger M. Continuous and discontinuous finite element methods for a peridynamics model of mechanics. Comput Methods Appl Mech Engrg 2011;200:1237-1250.

[4] Reji J, Surendra PS. Mixed-mode fracture of concrete subjected to impact loading. J Struct Eng 1990;116(3):585-602.

[5] Hu W, Wang Y, Yu J, Yen CF, Bobaru F. Impact damage on a thin glass plate with a thin polycarbonate backing. International Journal of Impact Engineering 2013;62:152-165.